PAPER

Au–Rh and Au–Pd nanocatalysts supported on rutile titania nanorods: structure and chemical stability†

Zere Konuspayeva,[a] Pavel Afanasiev,[a] Thanh-Son Nguyen,[a] Luca Di Felice,[a] Franck Morfin,[a] Nhat-Tai Nguyen,[b] Jaysen Nelayah,[b] Christian Ricolleau,[b] Z. Y. Li,[c] Jun Yuan,[d] Gilles Berhault[a] and Laurent Piccolo*[a]

Au, Rh, Pd, Au–Rh and Au–Pd nanoparticles (NPs) were synthesized by colloidal chemical reduction and immobilized on hydrothermally-prepared rutile titania nanorods. The catalysts were characterized by aberration-corrected TEM/STEM, XPS, and FTIR, and were evaluated in the hydrogenation of tetralin in the presence of H_2S. Oxidizing and reducing thermal treatments were employed to remove the polyvinyl alcohol (PVA) surfactant. Reduction in H_2 at 350 °C was found efficient for removing the PVA while preserving the size (*ca.* 3 nm), shape and bimetallic nature of the NPs. While Au–Pd NPs are alloyed at the atomic scale, Au–Rh NPs contain randomly distributed single-phase domains. Calcination–reduction of Au–Rh NPs mostly leads to separated Au and Rh NPs, while pre-reduction generates a well-defined segregated structure with Rh located at the interface between Au and TiO_2 and possibly present around the NPs as a thin overlayer. Both the titania support and gold increase the resistance of Rh and Pd to oxidation. Furthermore, although detrimental to tetralin hydrogenation initial activity, gold stabilizes the NPs against surface sulfidation in the presence of 50 ppm H_2S, leading to increased catalytic performances of the Au–Rh and Au–Pd systems as compared to their Rh and Pd counterparts.

1. Introduction

Nanoalloys are currently the subject of renewed interest due to the recent progress in atomic-scale characterization techniques, such as aberration-corrected transmission electron microscopy, together with a variety of applications of such systems to industrially-important catalytic reactions.[1,2] This progress has favored the development of new nanoalloy synthesis and structural modeling methods. In heterogeneous catalysis, a large fraction of reactions are catalyzed by metals, and the catalytic performances (activity, selectivity, stability) can often be improved by alloying. Traditionally categorized as either geometric or electronic effects, the catalytic synergies provided by alloying originate from a combination of factors, as in the case of strain effects.

Catalytic hydrogenation of aromatic hydrocarbons, for which palladium and rhodium are among the most efficient metals, forms an important class of reactions. They are used, *e.g.*, in petroleum refining to increase the combustion efficiency of fuels and reduce carcinogenic microparticle emissions.[3] In such applications, after deep hydrodesulfurization, the fuels still contain ppm amounts of sulfur, mostly in the form of H_2S. However, in spite of the nobleness of platinum-group metals, these materials readily react with S-containing species and strongly bond atomic sulfur, which possibly leads to metal sulfidation and irreversible poisoning.[4] Hence, the development of S-resistant hydrogenation catalysts is highly desirable. This goal can be achieved by using acidic supports, such as alumino-silicates, which induce electron transfers and thereby weaken the sulfur–metal bond.[5] Another approach consists in "nanoalloying" platinum-group metals with less reactive ones, such as gold, with the aim of increasing the catalyst stability.[2]

In this work, our first objective was to synthesize well-defined Au–Rh/TiO_2 catalysts using a facile preparation method similar to the one widely employed for Au–Pd nanoparticles, namely the colloidal synthesis. While Au–Pd is one of the most studied bimetallic systems due to its promising applications

[a] Institut de recherches sur la catalyse et l'environnement de Lyon (IRCELYON), UMR 5256 CNRS & Université Claude Bernard – Lyon 1, 2 avenue Albert Einstein, 69626 Villeurbanne, France. E-mail: laurent.piccolo@ircelyon.univ-lyon1.fr

[b] Laboratoire Matériaux et Phénomènes Quantiques (MPQ), UMR 7162 CNRS & Université Paris-Diderot, Bâtiment Condorcet, 4 rue Elsa Morante, 75205 Paris Cedex 13, France

[c] Nanoscale Physics Research Laboratory, School of Physics and Astronomy, University of Birmingham, Edgbaston, Birmingham B15 2TT, UK

[d] Department of Physics, University of York, Heslington, York, YO10 5DD, UK

in catalysis,[6–17] Au–Rh has been only scarcely investigated. From bulk thermodynamics, the Au–Pd and Au–Rh systems exhibit opposite behaviors. Au and Pd are fully miscible, as shown by the bulk phase diagram.[18] In contrast, Au and Rh have a positive mixing enthalpy (ΔH_{mix}^{Au-Rh} = 7 kJ mol^{-1} vs. ΔH_{mix}^{Au-Pd} = -8 kJ mol^{-1}), and a large difference in cohesion energies ($E_{coh}^{Rh} - E_{coh}^{Au}$ = 1.94 eV $\gg E_{coh}^{Pd} - E_{coh}^{Au}$ = 0.08 eV) and surface energies ($E_{surf}^{Rh} - E_{surf}^{Au}$ = 1.2 J m^{-2} $\gg E_{surf}^{Pd} - E_{surf}^{Au}$ = 0.6 J m^{-2}). They also present a larger difference in lattice constants ($a_{Au} - a_{Rh}$ = 0.28 Å > $a_{Au} - a_{Pd}$ = 0.19 Å).[19,20] As this combination of parameters drives the trends to alloying/ demixing and surface segregation,[21] it leads to a broad miscibility gap in the bulk Au–Rh phase diagram.[22] Consequently, as compared to that of Au–Pd nanoalloys, the case of Au–Rh is less favorable to alloying and the structure of Au–Rh nanoparticles is likely to depend much more strongly on the preparation conditions.

Kiss, Óvári and coworkers published the largest body of work on the Au–Rh system.[23–28] The authors synthesized Au–Rh particles or thin films supported on TiO$_2$ substrates of various forms (commercial powder, nanowires, nanotubes, and TiO$_2$(110) single-crystal). They used either chemical impregnation or physical vapor deposition, and a number of surface analysis techniques. It was shown that Au has a strong tendency to cover the Rh surface, and that Au inhibits the encapsulation of Rh by TiO$_x$ layers at high temperature. Recently, Chantry et al. investigated the growth of Pd and Rh on Au nanorods using aberration-corrected scanning transmission electron microscopy techniques. They showed that a randomly mixed alloy layer (4–5 atomic layers thick) forms between Au and Rh, in contrast to the sharp interface formed between the Au substrate and the Pd overlayer.[29–31] This observation seems to be in contradiction with thermodynamic data but in fact it highlights the importance of kinetics in governing the structure of nanoalloys.[30] Consistently, using colloidal methods and small materials amounts, Schaak and coworkers successfully synthesized alloy nanoparticles of various systems, including Au–Rh.[32] Finally, García et al. used microwave irradiation to synthesize Ag–Rh and Au–Rh nanoparticles (NPs) capped with poly(vinylpyrrolidone) and further deposited on amorphous silica.[33,34] Catalytic testing in cyclohexene hydrogenation at ambient temperature and pressure showed some activity enhancements for the bimetallic catalysts with respect to their monometallic counterparts.

In this paper, we present the synthesis, structural characterization, and catalytic evaluation of Au–Pd and Au–Rh NPs supported on rutile titania nanorods. The latter are used as an ideally shaped substrate for electron microscopy imaging. We focus on the system- and pretreatment-dependent chemical structure of the NPs as well as on their chemical reactivity toward oxygen and sulfur. In particular, the catalysts were tested in high-pressure hydrogenation of tetralin in the presence of traces of H$_2$S in order to assess the effect of Au addition on Pd and Rh thioresistance. The two bimetallic systems were compared to each other and to the monometallic systems with the aim of understanding the impact of the NP structure on their chemical stability.

2. Experimental

2.1. Preparation methods

TiO$_2$ rutile nanorods were prepared using a simplified procedure based on a hydrothermal method reported by Li and Afanasiev.[35] 10 g of commercial Degussa P25 TiO$_2$ (50 m^2 g^{-1}) and 100 mL of 15 wt% H$_2$SO$_4$ solution were mixed in a Teflon reactor and placed in a sealed autoclave kept at 200 °C for 15 days. The obtained solid was washed several times with 0.1 M NH$_4$NO$_3$ to remove adsorbed sulfate, then washed with distilled water, dried at 100 °C overnight, and calcined at 350 °C in air for 2 h.

Au–Pd and Au–Rh NPs, along with their monometallic counterparts, were prepared using a colloidal chemical (co)reduction route adapted from Toshima, Prati, Hutchings, and coworkers.[6–10] The metal precursors were HAuCl$_4$·3H$_2$O (Strem Chemicals, 99.9%, 49 wt% Au), RhCl$_3$·nH$_2$O (Sigma-Aldrich, 99.9%, 38–40 wt% Rh), and Na$_2$PdCl$_4$ (Sigma-Aldrich, 98%). In a first step, a 200 mL aqueous solution containing the two metallic precursors was prepared by adding the amounts of precursors necessary for reaching a total metal loading of 3 wt%. An Au$_{50}$Pd$_{50}$ composition as well as different Au–Rh compositions were envisaged. Next, a 1 wt% aqueous solution of a stabilizing agent, polyvinyl alcohol (PVA, M_w = 10 000) was added to the preceding solution while maintaining a mass ratio $m_{PVA}/m_{(Au+M)}$ of 1.2. A solution of 0.1 M NaBH$_4$, freshly prepared and kept at 0 °C before use, was then dropped under stirring in the solution of metallic precursors with a molar ratio $n_{NaBH_4}/n_{(Au+M)}$ of 5. Note that the use of tetrabutylammonium bromide (TBAB) instead of NaBH$_4$ led to NP size inhomogeneity. The excess of reducing agent was necessary to ensure a complete reduction of the two metals. Immediately after NaBH$_4$ addition, the color of the solution changed from yellowish orange to black, indicating the reduction of Au^{3+} and Rh^{3+}(Pd^{2+}) ions into Au^0 and Rh^0(Pd^0). Stirring was then maintained for 30 min to allow the complete decomposition of the remaining NaBH$_4$ excess. This stirring time, corresponding to NP nucleation and growth, had to be less than 1 h in the particular case of Au–Rh, since the corresponding colloids tend to agglomerate and precipitate, as observed by dynamic light scattering.[36] The solution was then acidified to pH 3.5 by addition of HCl 0.01 M in order to favor the sol immobilization onto the TiO$_2$ support. HCl was employed instead of frequently used H$_2$SO$_4$ as support acidifier, since the sulfur of H$_2$SO$_4$ was seen to deactivate the metal catalysts.[37] The amount of support necessary for reaching the final metal loading was then added and stirring was kept for 3 h. Finally, the material was filtrated, washed with hot distilled water (70 °C) several times, and dried at 100 °C overnight. The final washing of the catalysts with hot water enabled the removal of residual chloride.[38]

Ex situ treatments were applied using a dedicated bench in order to remove the PVA from the metal NP surface. These oxidizing (calcination) or reducing treatments were performed by heating the samples to 350 °C (10 °C min^{-1}, 3 h plateau) in air flow or hydrogen flow (5 mL min^{-1}, 1 atm), respectively. For FTIR and XPS characterization, the treatments could be applied *in situ* at the same temperature (see next section). Before the catalytic tests, the as-prepared ("fresh") catalysts were reduced

This journal is © the Owner Societies 2015

Phys. Chem. Chem. Phys., 2015, **17**, 28112–28120 | **28113**

in the reactor under pure hydrogen flow (90 mL min^{-1}) at 350 °C for 3 h.

2.2. Characterization methods

The metal weights were determined by inductively coupled plasma-optical emission spectroscopy (ICP-OES, Activa instrument from Horiba Jobin Yvon). In order to dissolve them completely, the samples were treated with a mixture of H_2SO_4, *aqua regia* and HF at 250–300 °C.

Routine transmission electron microscopy (TEM) experiments were performed with a JEM 2010 microscope (LaB$_6$ filament, 200 kV operating voltage), while advanced TEM characterization results were acquired using a JEM-ARM 200F equipped with a cold-field emission gun and an image aberration corrector.[39] In the present work, the microscope was operated at an accelerating voltage of 80 kV to limit radiation damage to the NPs. In addition, scanning transmission electron microscopy (STEM) observations were conducted using a JEM-2100F (FEG, 200 kV) equipped with a probe aberration corrector and a high-angle annular dark field (HAADF) detector. All three microscopes include energy dispersive X-ray (EDX) spectroscopy systems. For TEM observations, the samples were crushed in ethanol and the solution was ultrasonically stirred before dropping on a holey carbon-covered copper TEM grid, followed by drying. For STEM investigations, the samples were crushed in air using glass slides and the particles were drop casted on TEM grids.

Transmission infrared spectroscopy of adsorbed CO (CO-FTIR) was carried out using a Thermo Nicolet 6700 spectrometer (DTGS detector) combined with a new custom-made glass cell and a gas/vacuum handling system. The cell allows for *in situ* treatment (gas flow, 1 atm, RT-500 °C) of the samples, which can be moved vertically between the (upper) treatment and (bottom) analysis† positions with a magnetic transfer device. The cell can be evacuated down to *ca.* 10^{-5} Pa using a turbomolecular pump, and its bottom part can be cooled down to −196 °C (*ca.* −150 °C at the sample level) thanks to an included Pyrex Dewar system filled with liquid nitrogen (LN$_2$). CO (Air Liquide, purity 99.997%) can be dosed gradually and automatically using a stainless steel buffer and electro-valves. The samples were prepared in the form of self-supported pellets (13 mm diameter, *ca.* 500 μm thickness, *ca.* 20 mg weight, 2.5 tons mechanical pressure). The pellets were pretreated at 350 °C (5 °C min^{-1} from RT, 1 h plateau) in H$_2$ flow or 20% O$_2$/He flow (50 mL min^{-1}) when needed, and they were outgassed at 350 °C for 1 h under vacuum. Then, they were placed in analysis position and cooled down. A reference spectrum was recorded for the clean sample. Afterwards, cumulative dosing of CO (1 μmol per dose) and subsequent spectrum acquisition were performed until the moment when saturation coverage of CO was observed in the spectra. The spectra were recorded with 128 scans and 4 cm^{-1} resolution in the 4000–900 cm^{-1} range.

XPS analyses were carried out using an Axis Ultra DLD spectrometer from Kratos Analytical including a monochromatized Al K$_\alpha$ source (1486.6 eV). The analyzer was operated at 160 eV pass energy for acquisition of survey scans and at 40 eV pass energy for acquisition of high-resolution spectra. All peaks were calibrated using the Ti 2p$_{3/2}$ core level as the spectral reference, which was fixed at 458.8 eV. The instrument was equipped with an *in situ* high-temperature quartz reaction cell, which allowed us to pretreat the samples by heating them at 350 °C for 3 h under H$_2$ flow or O$_2$ flow (50 mL min^{-1}, 1 atm).

2.3. Catalytic testing method

High-pressure gas-phase tetralin hydrogenation tests were performed in a flow fixed bed reactor almost identical to an apparatus described in detail elsewhere.[5] The reactor itself was a stainless steel U-shape tube (4 mm internal diameter). Tetralin (Sigma-Aldrich, 99%) and hydrogen (Air Liquide, 99.999%) partial pressures were respectively 11 kPa and 4 MPa, and the total flow rate was 90 mL min^{-1} (NTP) with a catalyst weight of 15 mg. The catalyst thioresistance was evaluated by introducing an additional flow (10 mL min^{-1}) of a H$_2$S–H$_2$ mixture (Praxair, 500 ppm H$_2$S in H$_2$) to obtain 50 ppm of H$_2$S in the feed. Accordingly, in this case the tetralin partial pressure decreased to 10 kPa. The catalyst temperature was kept at 350 °C. Tetralin and reaction products (mainly *trans–cis* decalins, and traces of other C$_{10}$ products; no C$_9$ products were detected) were analyzed online using a Hewlett Packard 6890 gas chromatograph equipped with a flame ionization detector and an Agilent HP1 column (25 m × 0.2 mm × 0.5 μm).

3. Results and discussion

3.1. TiO$_2$ rutile nanorods

Rutile titania nanorods synthesized hydrothermally from P25 titania (see Section 2.1) were used as a well-defined and strongly-interacting support for the metal nanoparticles.[37] An X-ray diffractogram of the nanorods is shown in Fig. S1 (ESI†), revealing a pure rutile phase. Representative TEM images of the nanorods are reported in Fig. 1a and b. They present an oblong shape (100–300 nm length and 30–50 nm in width) with square cross section (see inset in Fig. 1a). The nanorods are oriented along the [001] axis and selectively expose 80–90% of (110) facets. The rod tips are formed mostly by (111) facets, but some rods have rounded terminations with no well-defined exposed plane. The specific surface area after heating at 350 °C in air is 30–35 m^2 g^{-1}.

3.2. TiO$_2$-supported Au–Pd and Au–Rh catalyst characterization by (S)TEM

Au–Pd and Au–Rh nanoalloys, along with their monometallic counterparts, were synthesized by a colloidal method, followed by sol immobilization on the titania support (Section 2.1). The metal loadings of the prepared samples are reported in Table 1. Aberration-corrected TEM images of the fresh Au$_{54}$Pd$_{46}$/TiO$_2$ sample are shown in Fig. 1c, while an aberration-corrected STEM-HAADF image of the fresh Au$_{63}$Rh$_{37}$/TiO$_2$ sample is shown in Fig. 2a. In any case, the catalysts exhibit a relatively sharp NP size distribution centered around 3 nm (Table 1 and Fig. 3), and the NPs are mostly faceted. However, as also observed by others,[10] the NPs are inhomogeneous in shape and atomic structure. Single-crystalline and twinned NPs are observed in each sample
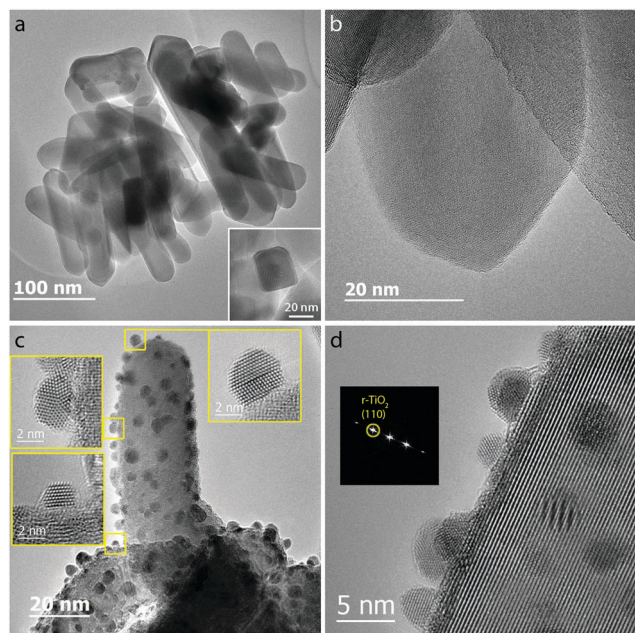
28114 | *Phys. Chem. Chem. Phys.*, 2015, **17**, 28112–28120

This journal is © the Owner Societies 2015

Fig. 1 Representative aberration-corrected TEM images of TiO$_2$ (a, b) and Au$_{46}$Pd$_{54}$/TiO$_2$ (c: fresh; d: reduced). Inset of (a) cross-sectional view of a nanorod. Insets of (c) HRTEM images of three nanoparticles (the facets are indexed in Fig. S2, ESI†). Inset of (d) FFT of an NP-free TiO$_2$ zone.

Fig. 2 Representative aberration-corrected STEM-HAADF images of Au$_{63}$Rh$_{37}$/TiO$_2$: (a, b) fresh sample; (c) reduced sample; (d) calcined-reduced sample. The arrows in (b) indicate signs of metal segregation.

Table 1 Metal content (ICP-OES) and metal particle size (TEM) of the as-prepared catalysts

Metal compos. (at%)	Metal loading (wt%)	NP size (nm)
Au	1.5	2.8 ± 0.8
Au	1.8	—
Pd	0.82	1.7 ± 0.7
Rh	0.64	—
Rh	0.62	2.4 ± 0.6
Au$_{46}$Pd$_{54}$	2.4	2.5 ± 1.0
Au$_{37}$Rh$_{63}$	2.4	3.2 ± 1.2
Au$_{55}$Rh$_{45}$	2.3	3.3 ± 1.0
Au$_{57}$Rh$_{43}$	2.2	4.0 ± 1.3
Au$_{63}$Rh$_{37}$	2.5	3.3 ± 1.0

(see insets of Fig. 1c, and Fig. S2, ESI†). Moreover, the NPs exhibit weak epitaxy on the support, *i.e.* numerous epitaxial relationships could be observed.

Both for Au–Pd and Au–Rh samples, local EDX analyses reveal the bimetallic nature of the NPs. However, the chemical structure depends on the bimetallic system. In the case of Au–Pd, TEM (Fig. 1c and d) as well as STEM and XRD[36] suggest the formation of a solid solution with random distribution of Au and Pd atoms. Unlike for Au–Pd NPs synthesized by physical vapor deposition,[40] no long-range chemical order is detected within the chemically synthesized NPs. For Au–Rh, the characterization results rule out an extensive atomic-scale alloying of Au and Rh atoms. Instead, STEM-HAADF images of Au$_{63}$Rh$_{37}$/TiO$_2$ (see Fig. 2b) and unsupported AuRh@PVA colloids[36] exhibit signs of metal phase segregation within the NPs. The Au-rich areas appear brighter than the Rh-rich ones. HAADF-STEM was performed under favorable conditions of Z-contrast on Au–Rh due to the large difference in atomic numbers (Z_{Au} = 79, Z_{Rh} = 45, intensity $\sim Z^{1.7}$).[41]

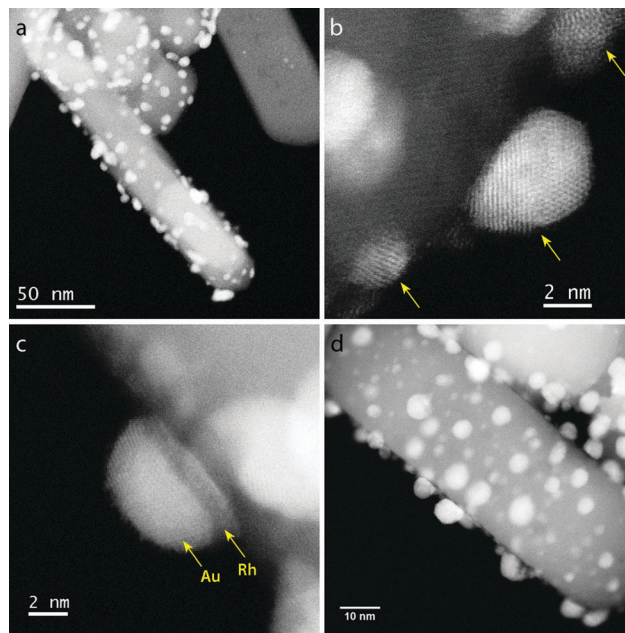The samples were exposed to oxidizing (air flow) and/or reducing (H$_2$ flow) thermal treatments in order to remove the PVA and thereby activate the catalysts. Low-temperature FTIR experiments in transmission mode performed on the Au$_{63}$Rh$_{37}$/TiO$_2$ sample show that both *in situ* reduction and calcination–reduction at 350 °C lead to surface dehydroxylation (Fig. 4a) and, most importantly, full removal of the adsorbed PVA (Fig. 4b). Indeed, the IR bands related to C–O and C–H vibrations in PVA[42] totally disappear upon treatments.

These treatments have no drastic influence on the NP size distributions, as shown by the size histograms of Fig. 3. In the case of Au$_{46}$Pd$_{54}$/TiO$_2$, the smallest particles (<2 nm) disappear upon treatments, and the size distribution becomes some-what sharper and centered on 2.9–3.0 nm instead of 2.5 nm (Fig. 3a). For Au$_{63}$Rh$_{37}$/TiO$_2$, the size distribution shifts to slightly larger mean sizes (from 3.3 to 3.7 nm) upon reduction or becomes somewhat broader and bimodal on calcination–reduction. The size standard deviation increases from 1.0 to 1.3 nm (Fig. 3b).

TEM (Fig. 1d) and XRD[36] do not show any significant change of the Au–Pd NP structure upon treatment, the NPs retaining their alloyed configuration in all cases. Conversely, the reducing treatment leads to a structural modification of the Au–Rh NPs, as evidenced by STEM. Indeed, as in the example of Fig. 2c, many of the NPs adopt a segregated "Janus-like" configuration, with Au/Rh/TiO$_2$ stacking. Note, however, that TEM and XRD[37] observations of amorphous "carbon black" powders highly loaded with AuRh NPs reveal partial intermixing between Au and Rh after reducing treatment. Finally, the calcination–reduction treatment (Fig. 2d) mostly leads to full metal segregation, with separated (smaller) Rh and (bigger) Au NPs, as determined from lattice parameter measurements on several images.
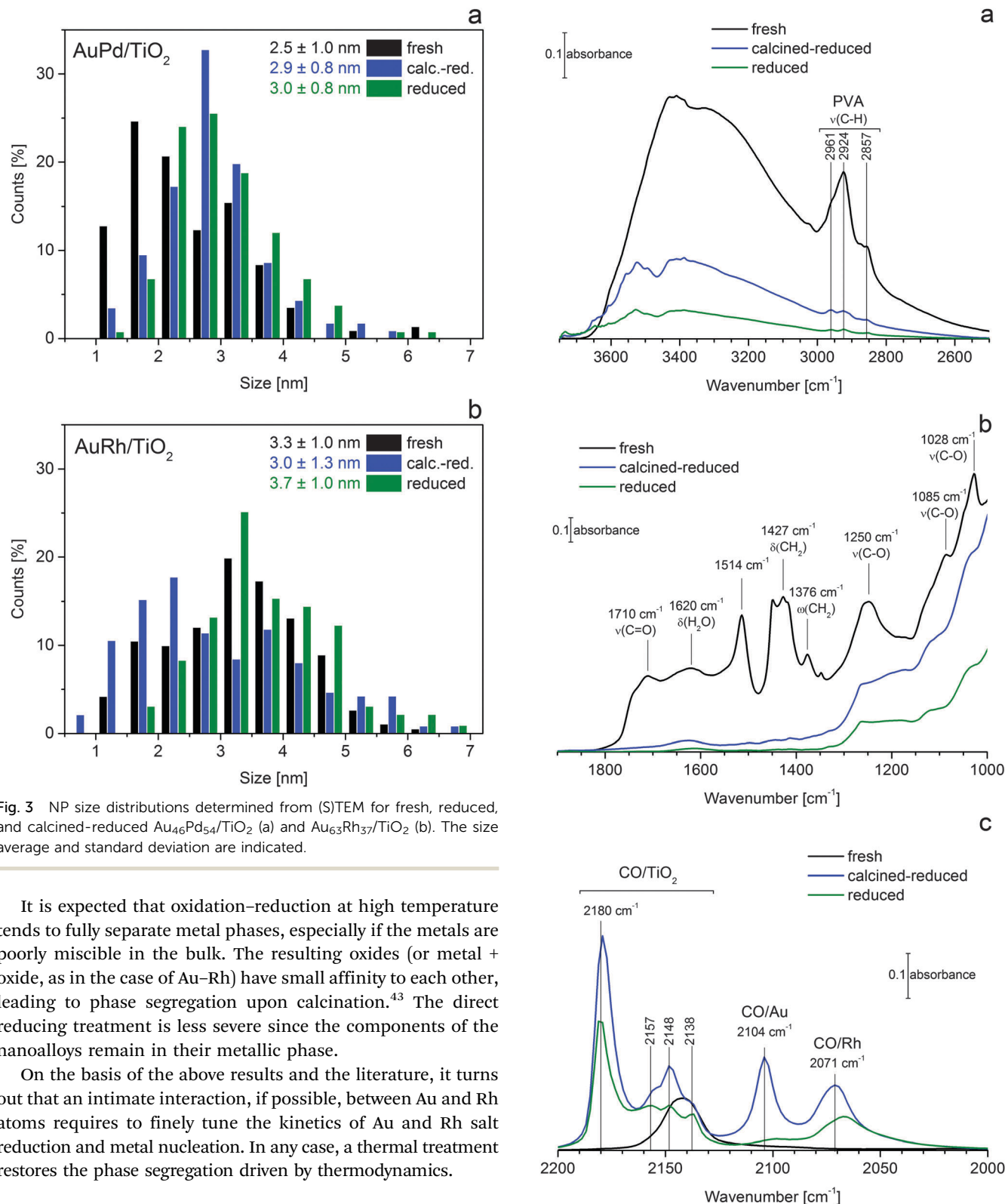
This journal is © the Owner Societies 2015

Phys. Chem. Chem. Phys., 2015, **17**, 28112–28120 | **28115**

Fig. 3 NP size distributions determined from (S)TEM for fresh, reduced, and calcined-reduced $Au_{46}Pd_{54}/TiO_2$ (a) and $Au_{63}Rh_{37}/TiO_2$ (b). The size average and standard deviation are indicated.

It is expected that oxidation–reduction at high temperature tends to fully separate metal phases, especially if the metals are poorly miscible in the bulk. The resulting oxides (or metal + oxide, as in the case of Au–Rh) have small affinity to each other, leading to phase segregation upon calcination.[43] The direct reducing treatment is less severe since the components of the nanoalloys remain in their metallic phase.

On the basis of the above results and the literature, it turns out that an intimate interaction, if possible, between Au and Rh atoms requires to finely tune the kinetics of Au and Rh salt reduction and metal nucleation. In any case, a thermal treatment restores the phase segregation driven by thermodynamics.

3.3. AuRh nanoparticle surface phase determination by CO-FTIR

The $Au_{63}Rh_{37}/TiO_2$ sample, either as-prepared or subjected to *in situ* pre-reduction/calcination–reduction at 350 °C, was characterized by FTIR spectroscopy after evacuating the cell and dosing a small amount of CO (which corresponds to saturation

Fig. 4 FTIR spectra recorded at −196 °C for $Au_{63}Rh_{37}/TiO_2$ after introduction of 4.2 µmol CO: (a) hydroxyl region; (b) PVA region; (c) carbonyl region. The treatments at 350 °C were applied *in situ*.

coverage on the metals) at LN_2 temperature. The results are presented in Fig. 4c. The IR band assignments are based on

published results for TiO_2,[44–47] Au[45–47] and Rh,[48–52] and on comparison to similar experiments performed on pure TiO_2, Au/TiO_2 and Rh/TiO_2 samples.[36]

The bands at 2180 cm^{-1} and 2157 cm^{-1} (both absent for the fresh sample) are related to CO chemisorbed on β'' Ti^{4+} Lewis acid sites and CO physisorbed on Ti–OH sites, respectively, while the bands at 2148 cm^{-1} and 2138 cm^{-1} correspond to CO physisorption on TiO_2.[44–46]

While the fresh sample exhibits no metal–CO IR band, intense bands at 2104 cm^{-1} and 2071 cm^{-1}, corresponding to Au^0–CO (2105 cm^{-1} for Au/TiO_2) and Rh^0–CO (2069 cm^{-1} for Rh/TiO_2), respectively, are present for the calcined-reduced sample. This result is consistent with the above-mentioned STEM observations showing separated Au and Rh particles after calcination–reduction.

The reduced sample shows a broad band centered at 2067 cm^{-1} and a very small one near 2100 cm^{-1}, suggesting the quasi absence of gold at the surface. The comparison with STEM results further suggests that Janus-like NPs are surrounded by a thin Rh envelope. This hypothesis might seem contradictory with the above-mentioned lower surface energy of Au as compared to Rh, but it is in fact fully consistent with adsorption-induced surface segregation of the more reactive element.[2]

Additional CO-FTIR experiments on calcined $Au(Rh)/TiO_2$ samples show a distinct IR band centered at 2120 cm^{-1} only for Au/TiO_2 (Fig. S3, ESI†). This band is assigned to cationic gold ($Au^{\delta+}$).[45] Hence, the presence of Rh may prevent Au from being: (i) oxidized during calcination and/or (ii) stabilized as $Au^{\delta+}$ in contact with TiO_2. This is consistent with a Rh shell (i) and/or the location of Rh at the interface between Au and TiO_2 demonstrated by STEM-HAADF images (ii).

3.4. Nanoalloy near-surface characterization by XPS

All the supported samples, either as-prepared or pre-oxidized–reduced at 350 °C, were analyzed by XPS. An unsupported AuRh@PVA sample was also analyzed for comparison. The spectra for Au 4f, Pd 3d and Rh 3d core levels are shown in Fig. 5.

The presence of TiO_2 induces a downshift in the binding energy of the Au 4f and Rh 3d core levels, with respect to AuRh@PVA. For the latter, the Au $4f_{7/2}$ (84.1 eV) and Rh $3d_{5/2}$ (307.2 eV) peak positions agree well with bulk Au^0 (83.95 eV) and Rh^0 (307.2 eV) reference values,[53] respectively. The downshift by 0.4–0.7 eV observed for TiO_2-supported samples can be ascribed to electron transfer from titania to the metal.[54]

The $AuPd/TiO_2$ samples show downshifts of Au 4f (0.4 eV) and Pd 3d (0.3–0.8 eV) core levels as compared to the Au/TiO_2 and Pd/TiO_2 cases. This is consistent with the Au–Pd atomic-scale alloying mentioned above.[11] It was previously explained by a charge compensation model in which Pd donates sp electrons to Au while Au donates d electrons to Pd.[55] The $AuRh/TiO_2$ samples exhibit only slight downshifts of the Au 4f (<0.3 eV) and Rh 3d (<0.2 eV) core levels with respect to their Au/TiO_2 and Rh/TiO_2 counterparts, consistent with the limited extent of Au–Rh atomic-scale alloying mentioned previously.

With respect to pre-reduced Pd/TiO_2 and $AuPd/TiO_2$ samples showing only a Pd^0 contribution at the Pd $3d_{3/2}$ core level,
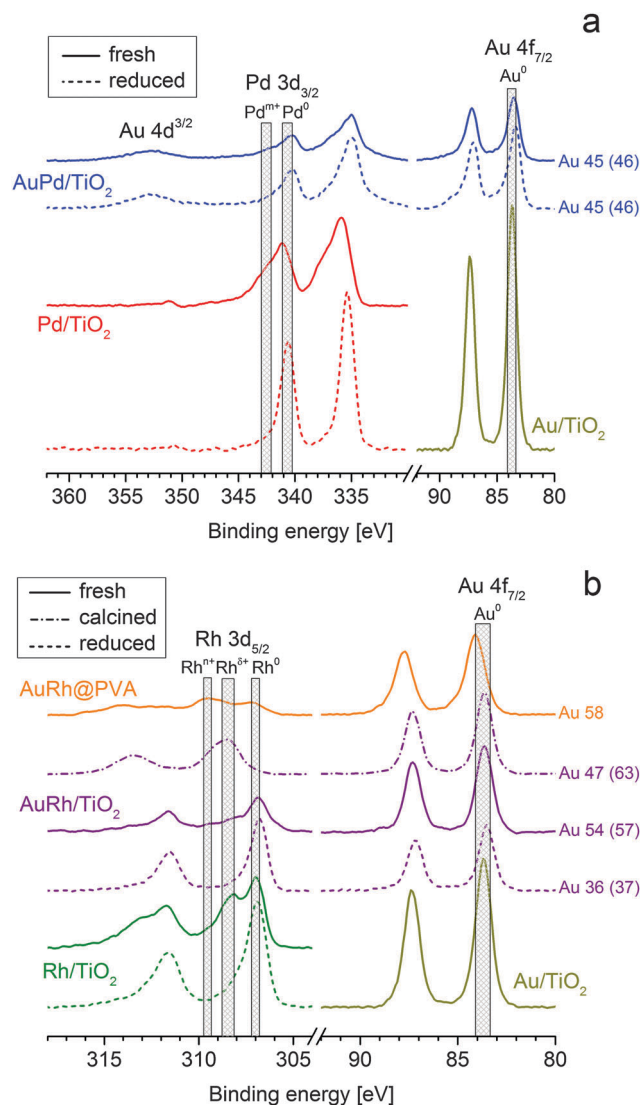

Fig. 5 XPS spectra for AuRh@PVA (fresh) and TiO_2-supported Au, Pd, Rh, $Au_{46}Pd_{54}$, $Au_{37}Rh_{63}$, $Au_{57}Rh_{43}$, and $Au_{63}Rh_{37}$ catalysts (fresh, calcined, or reduced): (a) Au, Pd and Au–Pd samples; (b) Au, Rh and Au–Rh samples. The hatched rectangles indicate the ranges of peak positions. Each spectrum was normalized by the total area of metal contributions. The numbers at the right-hand side give the Au concentrations (at%) determined by XPS. The values between brackets are the Au concentrations determined by elemental analysis of the samples.

the fresh samples exhibit an additional contribution (denoted Pd^{m+} in Fig. 5a, $m \approx 2$) at higher binding energy, which corresponds to oxidized Pd.[17] Note that the Pd $3d_{5/2}$ core level is close to the Au $4d_{5/2}$ one, which prevents us from using the 5/2 levels for the comparison between AuPd and Pd. Interestingly, the fraction of Pd^{m+} is much smaller in the case of AuPd, suggesting a stabilizing effect of Au on Pd oxidation in air. A similar effect is shown in Fig. 5b for Rh and AuRh samples: the latter exhibit proportionally smaller Rh oxide contributions (two $Rh^{\delta+}$ and Rh^{n+} oxidation states are present, with $\delta < n$, $n = 3$ or 4)[23,27,53] than the Rh samples. These contributions are well observed on the pre-calcined sample, while they are absent for the reduced samples. Furthermore, comparing the Rh 3d signals for fresh AuRh@PVA

This journal is © the Owner Societies 2015

Phys. Chem. Chem. Phys., 2015, **17**, 28112–28120 | **28117**

and AuRh/TiO$_2$ samples in Fig. 5b, it is seen that the Rh oxide fractions are much larger in the former case (with [Rh^{n+}] > [Rh$^{\delta+}$]). This also suggests an inhibiting effect of the titania support on Rh oxidation or a partial reduction of Rh oxides upon NP deposition on titania.

Finally, the quantification shows that Au/Pd and Au/Rh ratios agree with those determined by elemental analysis within 6% (Fig. 5). The only exception is the calcined Au–Rh sample which exhibits an enrichment in Rh, suggesting a possible core–shell Au@RhO$_x$ restructuring. However, it should be noticed that the electron mean free path being of 1.7 nm for Au, 1.9 nm for Rh, and 2.5 nm for Pd at the X-ray primary energy of 1486.6 eV,[56] and the NP dimension being of *ca.* 3 nm, both the bulk and the surface of the NPs are probed by XPS.

3.5. Evaluation of the catalysts for tetralin hydrogenation in the presence of H$_2$S

The catalytic tests were performed in the gas phase using a flow fixed bed reactor at high H$_2$ pressure (4 MPa) and 350 °C. The tests were preceded by *in situ* pretreatment of the fresh samples under pure hydrogen flow at 4 MPa for 3 h at 350 °C. *trans*-decalin and *cis*-decalin are the only reaction products, *i.e.*, tetralin is fully hydrogenated in these conditions. Fig. 6a shows the evolution of tetralin conversion with time-on-stream on the titania-supported catalysts. Note that Au/TiO$_2$ exhibited negligible activity (not shown here). The initial gradual decrease of the conversion is due to slow poisoning of the metal surface by sulfur impurities present in the reactor, even before addition of H$_2$S to the reaction feed. However, this decrease is slower on Rh-based catalysts than on Pd-based ones. Furthermore, with respect to Rh/TiO$_2$, the deactivation rate is smaller for Au$_{36}$Rh$_{64}$/TiO$_2$, and negligible for Au$_{57}$Rh$_{43}$/TiO$_2$, suggesting a stabilizing effect of Au on Rh.

Upon addition of H$_2$S, Pd/TiO$_2$ immediately loses part of its activity, then gradually deactivates. Going back to S-free conditions, the catalyst somewhat regenerates and stabilizes. AuPd/TiO$_2$ shows a different behavior since H$_2$S has initially a beneficial effect on the activity. We ascribe these results to the sulfidation of Pd in contact with H$_2$S. In our conditions, the Pd$_4$S phase, which is known to possess poor aromatics hydrogenation efficiency,[14] is most likely formed.[57] Alloying with Au seems to prevent Pd sulfidation, in agreement with previous works.[13,14]

Rh/TiO$_2$ has a radically different behavior as compared to Pd-based catalysts: the addition of H$_2$S is seen to continuously activate the catalyst, suggesting a highly active Rh sulfide phase. The gradual decrease of the conversion without H$_2$S in the feed could be the result of slow poisoning of the metal surface by strong adsorption of the reactants, the reaction products, or H$_2$S. Most probably, the role of sulfur impurities, causing the formation of a less sulfided Rh surface phase with poor activity, cannot be ruled out. In contrast, for the two Au–Rh/TiO$_2$ catalysts, H$_2$S has a limited influence on the conversion rate, and the activity only slightly decreases over 35 h of reaction. Hence, the addition of Au limits the influence of H$_2$S on Rh, as for the case of Pd.

Fig. 6b summarizes the results for the Rh-based catalysts in terms of *trans*/*cis* decalin selectivity and activity per Rh weight
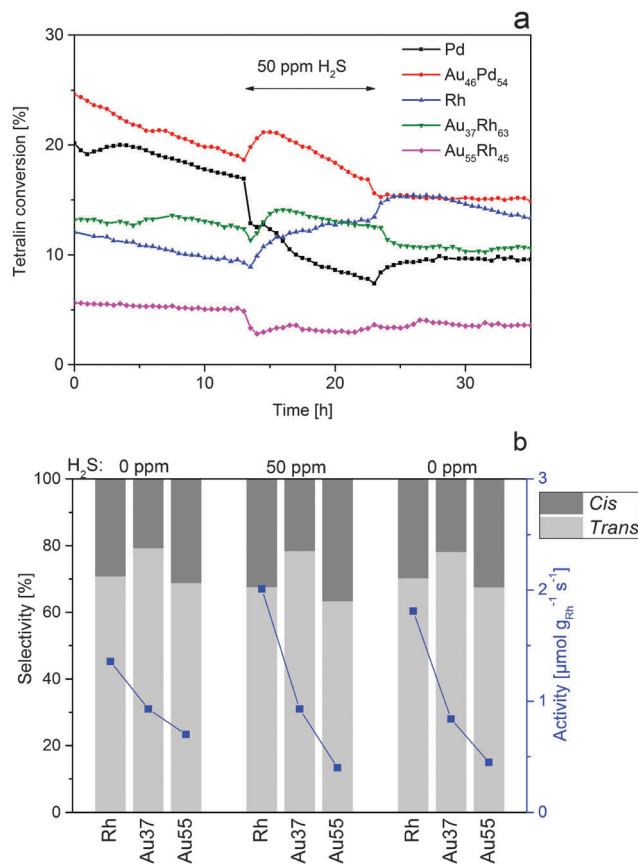

Fig. 6 (a) Tetralin conversion *versus* time on the TiO$_2$-supported catalysts without and with 50 ppm H$_2$S in the tetralin-hydrogen feed. (b) Tetralin conversion activity (blue square dots, right Y axis) and selectivity to *cis*- and *trans*-decalins (grey bars, left Y axis) of (Au-) Rh/TiO$_2$ catalysts at quasi steady state.

at quasi steady state. The *trans*/*cis* ratio, comprised between 1.7 and 3.8, is much lower than its value at thermodynamic equilibrium in our pressure and temperature conditions (6.7). The tetralin hydrogenation activity strongly decreases as the gold concentration increases, similarly to the findings of García *et al.* for cyclohexene hydrogenation,[34] suggesting that Au partially blocks hydrogenation sites.

4. Conclusion

The XPS and catalysis results point to a stabilizing effect of gold on the oxidation and sulfidation resistance of the Pt-group metals, respectively. In the case of Au–Pd nanoalloys, which exhibit solid-solution structure, this phenomenon can be confidently ascribed to the atomic-scale interaction between the two metals through electronic effects. In particular, the H$_2$S dissociation barrier is much higher and the sulfur adsorption energy much lower on Au than on the Pt-group metals.[58] The case of Au–Rh is more intriguing since STEM observations evidence at least partially segregated phases for the as-prepared catalysts and an Au/Rh/TiO$_2$ stacked segregated structure for the pre-reduced ones. However, the somewhat detrimental effect of

28118 | *Phys. Chem. Chem. Phys.*, 2015, **17**, 28112–28120

This journal is © the Owner Societies 2015

gold on tetralin hydrogenation activity shows that the catalyst may retain the latter structure under severe reducing reaction conditions, a thick gold layer protecting in part the Rh phase from sulfidation by H_2S. Further investigations of the Au–Rh/TiO_2 system are currently undertaken to rationalize the observed structures and the gold stabilizing effect.

Acknowledgements

References

1 R. Ferrando, J. Jellinek and R. L. Johnston, *Chem. Rev.*, 2008, **108**, 845–910.

2 L. Piccolo, in *Nanoalloys: Synthesis, Structure and Properties, Engineering Materials*, ed. D. Alloyeau, C. Mottet and C. Ricolleau, Springer-Verlag, London, 2012, pp. 369–404.

3 A. Stanislaus and B. H. Cooper, *Catal. Rev.: Sci. Eng.*, 1994, **36**, 75–123.

4 C. H. Bartholomew, P. K. Agrawal and J. R. Katzer, *Adv. Catal.*, 1982, **31**, 135–242.

5 S. Nassreddine, L. Massin, M. Aouine, C. Geantet and L. Piccolo, *J. Catal.*, 2011, **278**, 253–265.

6 N. Toshima, M. Harada, Y. Yamazaki and K. Asakura, *J. Phys. Chem.*, 1992, **96**, 9927–9933.

7 N. Toshima, *Pure Appl. Chem.*, 2000, **72**, 317–325.

8 N. Dimitratos, F. Porta and L. Prati, *Appl. Catal., A*, 2005, **291**, 210–214.

9 N. Dimitratos, J. A. Lopez-Sanchez, D. Morgan, A. F. Carley, R. Tiruvalam, C. J. Kiely, D. Bethell and G. J. Hutchings, *Phys. Chem. Chem. Phys.*, 2009, **11**, 5142–5153.

10 G. J. Hutchings and C. J. Kiely, *Acc. Chem. Res.*, 2013, **46**, 1759–1772.

11 C.-W. Yi, K. Luo, T. Wei and D. W. Goodman, *J. Phys. Chem. B*, 2005, **109**, 18535–18540.

12 F. Gao and D. W. Goodman, *Chem. Soc. Rev.*, 2012, **41**, 8009–8020.

13 A. M. Venezia, V. La Parola, V. Nicolì and G. Deganello, *J. Catal.*, 2002, **212**, 56–62.

14 B. Pawelec, A. M. Venezia, V. La Parola, E. Cano-Serrano, J. M. Campos-Martin and J. L. G. Fierro, *Appl. Surf. Sci.*, 2005, **242**, 380–391.

15 L. Piccolo, A. Piednoir and J.-C. Bertolini, *Surf. Sci.*, 2005, **592**, 169–181.

16 A. Hugon, L. Delannoy, J.-M. Krafft and C. Louis, *J. Phys. Chem. C*, 2010, **114**, 10823–10835.

17 Z. Zhang, S.-W. Cao, Y. Liao and C. Xue, *Appl. Catal., B*, 2015, **162**, 204–209.

18 H. Okamoto and T. B. Massalski, *Bull. Alloy Phase Diagrams*, 1985, **6**, 229–235.

19 F. R. de Boer, R. Boom, W. C. M. Mattens, A. R. Miedema and A. K. Niessen, *Cohesion in Metals: Transition Metal Alloys*, North-Holland Physics Publishing, 1989.

20 L. Vitos, A. V. Ruban, H. L. Skriver and J. Kollár, *Surf. Sci.*, 1998, **411**, 186–202.

21 J. Creuze, I. Braems, F. Berthier, C. Mottet, G. Tréglia and B. Legrand, *Phys. Rev. B: Condens. Matter Mater. Phys.*, 2008, **78**, 075413.

22 H. Okamoto and T. B. Massalski, *Bull. Alloy Phase Diagrams*, 1984, **5**, 384–387.

23 J. Raskó, Á. Koós, K. Baán and J. Kiss, *React. Kinet. Catal. Lett.*, 2007, **90**, 187–195.

24 L. Óvári, L. Bugyi, Z. Majzik, A. Berkó and J. Kiss, *J. Phys. Chem. C*, 2008, **112**, 18011–18016.

25 L. Óvári, A. Berkó, N. Balázs, Z. Majzik and J. Kiss, *Langmuir*, 2009, **26**, 2167–2175.

26 A. Kukovecz, G. Potari, A. Oszko, Z. Konya, A. Erdohelyi and J. Kiss, *Surf. Sci.*, 2011, **605**, 1048–1055.

27 J. Kiss, L. Óvári, A. Oszkó, G. Pótári, M. Tóth, K. Baán and A. Erdóhelyi, *Catal. Today*, 2012, **181**, 163–170.

28 L. Óvári, A. Berkó, R. Gubó, Á. Rácz and Z. Kónya, *J. Phys. Chem. C*, 2014, **118**, 12340–12352.

29 R. L. Chantry, W. Siriwatcharapiboon, S. L. Horswell, A. J. Logsdail, R. L. Johnston and Z. Y. Li, *J. Phys. Chem. C*, 2012, **116**, 10312–10317.

30 R. L. Chantry, I. Atanasov, W. Siriwatcharapiboon, B. P. Khanal, E. R. Zubarev, S. L. Horswell, R. L. Johnston and Z. Y. Li, *Nanoscale*, 2013, **5**, 7452–7457.

31 R. L. Chantry, I. Atanasov, S. L. Horswell, Z. Y. Li and R. L. Johnston, in *Gold Clusters Colloids and Nanoparticles II*, ed. D. M. P. Mingos, Springer International Publishing, 2014, pp. 67–90.

32 E. R. Essinger-Hileman, D. DeCicco, J. F. Bondi and R. E. Schaak, *J. Mater. Chem.*, 2011, **21**, 11599–11604.

33 S. García, R. M. Anderson, H. Celio, N. Dahal, A. Dolocan, J. Zhou and S. M. Humphrey, *Chem. Commun.*, 2013, **49**, 4241–4243.

34 S. García, L. Zhang, G. W. Piburn, G. Henkelman and S. M. Humphrey, *ACS Nano*, 2014, **8**, 11512–11521.

35 H. Li and P. Afanasiev, *Mater. Res. Bull.*, 2011, **46**, 2506–2514.

36 L. Piccolo, *et al.*, to be published.

37 Z. Konuspayeva, G. Berhault, P. Afanasiev, T.-S. Nguyen, A. Auyezov, M. Burkitbayev and L. Piccolo, in *MRS Proceedings*, MRS Online Proceedings Library, 2014, vol. 1641, mrsf13-1641-aa08-07.

This journal is © the Owner Societies 2015

Phys. Chem. Chem. Phys., 2015, **17**, 28112–28120 | **28119**

38 Z. Konuspayeva, PhD thesis, Université Claude Bernard – Lyon 1, 2014.

39 C. Ricolleau, J. Nelayah, T. Oikawa, Y. Kohno, N. Braidy, G. Wang, F. Hue, L. Florea, V. P. Bohnes and D. Alloyeau, *Microscopy*, 2013, **62**, 283–293.

40 J. Nelayah, N. T. Nguyen, D. Alloyeau, G. Y. Wang and C. Ricolleau, *Nanoscale*, 2014, **6**, 10423.

41 Z. Y. Li, in *Frontiers of Nanoscience*, ed. J. P. Wilcoxon and R. L. Johnston, Elsevier, 2012, vol. 3, pp. 213–247.

42 T. Nedoseykina, P. Plyusnin, Y. Shubin and S. Korenev, *J. Therm. Anal. Calorim.*, 2010, **102**, 703–708.

43 S. Zhou, H. Yin, V. Schwartz, Z. Wu, D. Mullins, B. Eichhorn, S. H. Overbury and S. Dai, *ChemPhysChem*, 2008, **9**, 2475–2479.

44 K. Hadjiivanov, *Appl. Surf. Sci.*, 1998, **135**, 331–338.

45 F. Boccuzzi and A. Chiorino, *J. Phys. Chem. B*, 2000, **104**, 5414–5416.

46 H. Klimev, K. Fajerwerg, K. Chakarova, L. Delannoy, C. Louis and K. Hadjiivanov, *J. Mater. Sci.*, 2007, **42**, 3299–3306.

47 L. Piccolo, H. Daly, A. Valcarcel and F. C. Meunier, *Appl. Catal., B*, 2009, **86**, 190–195.

48 M. Primet, *J. Chem. Soc., Faraday Trans. 1*, 1978, **74**, 2570–2580.

49 J. T. Yates, T. M. Duncan, S. D. Worley and R. W. Vaughan, *J. Chem. Phys.*, 1979, **70**, 1219–1224.

50 F. Solymosi and M. Pasztor, *J. Phys. Chem.*, 1985, **89**, 4789–4793.

51 L. L. Sheu and W. M. H. Sachtler, *J. Mol. Catal.*, 1993, **81**, 267–278.

52 S. Trautmann and M. Baerns, *J. Catal.*, 1994, **150**, 335–344.

53 *NIST X-ray Photoelectron Spectroscopy Database, Version 4.1*, National Institute of Standards and Technology, Gaithersburg, 2012, http://srdata.nist.gov/xps/.

54 A. Zwijnenburg, A. Goossens, W. G. Sloof, M. W. J. Crajé, A. M. van der Kraan, L. J. de Jongh, M. Makkee and J. A. Moulijn, *J. Phys. Chem. B*, 2002, **106**, 9853–9862.

55 Y. S. Lee, Y. Jeon, Y. D. Chung, K. Y. Lim, C. N. Whang and S. J. Oh, *J. Korean Phys. Soc.*, 2000, **37**, 451–455.

56 C. J. Powell and A. Jablonski, *NIST Electron Inelastic-Mean-Free-Path Database, Version 1.2, SRD 71*, National Insititute of Standards and Technology, Gaithersburg, MD, 2010.

57 E. J. M. Hensen, H. J. A. Brans, G. M. H. J. Lardinois, V. H. J. de Beer, J. A. R. van Veen and R. A. van Santen, *J. Catal.*, 2000, **192**, 98–107.

58 D. R. Alfonso, *Surf. Sci.*, 2008, **602**, 2758–2768.